Anomalous Northward Energy Transport due to Anthropogenic Aerosols during the Twentieth Century

MICHAEL R. NEEDHAM[a] AND DAVID A. RANDALL[a]

[a] *Department of Atmospheric Science, Colorado State University, Fort Collins, Colorado*

(Manuscript received 26 October 2022, in final form 5 June 2023, accepted 10 June 2023)

ABSTRACT: In the tropics, the absorbed solar radiation is larger than the outgoing longwave radiation, while the opposite is true at high latitudes. This basic fact implies a poleward energy transport (PET) in both hemispheres, which is accomplished by the atmosphere and oceans. The magnitude of PET is determined by the top of atmosphere gradient in the net radiation flux, and small changes to this quantity must change the total PET in the absence of changes in heat uptake. We analyze a large ensemble of 50 historic climate simulations from the CESM LENS2 project and find a significant PET anomaly in the latter half of the twentieth century. The temporal evolution of this anomaly—with a rapid increase after 1950, a peak near 1975, and a rapid decrease in the 1990s—mirrors the historic trend of sulfur dioxide (SO_2, a significant aerosol predecessor) emissions from Europe and North America. This anomaly also appears in an analysis of the PET calculated from ERA5 reanalyses and from the CESM2 Single Forcing Large Ensemble. Consistent with previous studies, we find that historic SO_2 emissions from Europe and North America brightened clouds, which reflected additional solar radiation back to space in the midlatitudes: this shortwave anomaly increased the meridional gradient in the net TOA radiation flux and induced an anomalous northward energy transport. Finally, our results suggest that cryosphere processes become an additional important factor in setting the PET anomaly during the first years of the twenty-first century by contributing to the difference in absorbed solar radiation between hemispheres alongside cloud radiative effects.

SIGNIFICANCE STATEMENT: In this study, we analyze a large group of climate model simulations from 1850 to 2014 and find that this historical pollution changed the way that heat was transported from the tropics to Earth's poles. We also find this change in heat transport when we analyzed an atmospheric reanalysis, which is a historical dataset that combines many meteorological observations into a best estimate of the past climate state. This extra reflection of sunlight from polluted clouds cooled the Northern Hemisphere, and we hypothesize that this cooling caused more heat transport out of the tropics. Last, we find that similar pollution emitted from China and India in more recent decades has not led to a change in Earth's heat transport because of counteracting changes in snow and ice in the Northern Hemisphere.

KEYWORDS: Energy transport; Energy budget/balance; Aerosol radiative effect

1. Introduction

Poleward energy transport (PET) is the necessary result of the meridional gradient in the TOA radiation flux between the tropics and the poles, and has been well understood for decades (Sverdrup et al. 1942; Riehl and Malkus 1958; Bjerknes 1964; Oort 1971; Vonder Haar and Oort 1973; Trenberth 1979). This PET is almost entirely accomplished through atmospheric and oceanic transports (Held 2001; Trenberth and Stepaniak 2004), with only a small residual occurring via other geophysical processes such as river and groundwater flows and iceberg transports. Stone (1978) showed that for an arbitrary spherical planet, the total poleward energy transport is determined by orbital parameters (i.e., axial tilt, eccentricity, and obliquity), the OLR, and the planetary albedo. This then implies that the total PET is largely insensitive to the specifics of atmospheric and oceanic dynamics inasmuch as they do not alter the meridional albedo gradient through changes in, for example, cloud properties or polar ice. Recent work has supported this interpretation, with several studies examining the role of polar ice in determining the total PET through changes in the albedo (Enderton and Marshall 2009; Rose and Ferreira 2012; Knietzsch et al. 2015; Shaw and Smith 2022). While it may seem an abstract concept, the PET is tied to many aspects of weather and climate, from the Arctic amplification of global warming (Hwang et al. 2011; Serreze and Barry 2011; Screen et al. 2012; Huang et al. 2017; Previdi et al. 2021; Pithan and Jung 2021) to the position of the intertropical convergence zone (ITCZ; Chiang and Bitz 2005; Kang et al. 2008; Marshall et al. 2013; Hwang et al. 2013; Frierson et al. 2013; Schneider et al. 2014; Adam et al. 2016; Donohoe and Voigt 2017; Kang 2020; Yukimoto et al. 2022).

An obvious question to consider is how the PET (and its constituent transports in the atmosphere and ocean) may respond to various climate forcings. For example, under greenhouse gas forcing the atmospheric energy transport is expected to increase due to increased latent energy transport by baroclinic eddies in a warmer atmosphere that holds more moisture (Held and Soden 2006; Hwang and Frierson 2010). Conversely, greenhouse warming may lead to a reduction in ocean energy transport due to a slowdown in the Atlantic meridional overturning circulation (Rahmstorf et al. 2015; Caesar et al. 2018, 2021) in

---

Corresponding author: Michael R. Needham, m.needham@colostate.edu

DOI: 10.1175/JCLI-D-22-0798.1

response to increased freshwater runoff into the North Atlantic from Greenland.

Anthropogenic aerosols also represent a major climate forcing with the same approximate global mean magnitude as, and opposite sign of, greenhouse gases (Fig. 2.10 from Gulev et al. 2021). However, aerosols typically have a much shorter lifetime than greenhouse gases, and thus are not well mixed in the atmosphere. In practice, this means that the radiative impact of aerosols can be extremely heterogeneous in space, and the resulting climate impact is sensitive to the location of emission (Shindell et al. 2010; Persad and Caldeira 2018).

The historic trend in anthropogenic aerosol concentrations is of primary relevance to this study, which we investigate through the related trend sulfur dioxide (SO_2) emissions. While there are natural sources (especially volcanoes; Gulev et al. 2021), SO_2 is a major pollutant, with a large fraction of emissions from the energy extraction and industrial sectors of the economy (Hoesly et al. 2018). In the atmosphere, SO_2 is oxidized to sulfuric acid (H_2SO_4), a major contributor to acid rain (Grennfelt et al. 2020). In the presence of ammonia (NH_3) or other alkaline agents, H_2SO_4 is neutralized to form sulfate aerosol (Larssen et al. 2006); sulfate aerosols impact the climate directly by scattering radiation, and indirectly through changes in clouds and precipitation (Twomey 1977; Albrecht 1989; Rosenfeld et al. 2014; Hoesly et al. 2018; Naik et al. 2021).

The Community Emissions Data System (CEDS; Hoesly et al. 2018), used as one of the forcing agents for the Coupled Model Intercomparison Project, Phase 6 (CMIP6; Eyring et al. 2016), records our current best estimate of the trend in SO_2 emissions from 1750 to the near-present. SO_2 emissions increased rapidly in the decades following World War II, mirroring the trend exhibited by all pollutants. However, in contrast to pollutants like CO_2, SO_2 emissions began to decline in Europe and North America in the last quarter of the twentieth century due to emission control policies. As emissions declined in Europe and North America, the primary source region shifted to Asia (see Figs. 2 and 3 of Hoesly et al. 2018), which is presently responsible for around half of annual SO_2 emissions. Recent studies have suggested that this increase and then decline in SO_2 emissions from the industrialized West has enhanced the cooling during the mid-twentieth century and has contributed to the recently observed amplification of warming in the Arctic (Acosta Navarro et al. 2016; Deser et al. 2020; England et al. 2021; Aizawa et al. 2022).

Hwang et al. (2013) found that historic aerosol emissions shifted the ITCZ southward in the late twentieth century. They proposed a mechanism whereby aerosol direct and indirect effects decrease local solar absorption in the northern midlatitudes, which induces an anomalous Hadley circulation. The upper branch transports anomalous dry static energy (DSE; the combination of potential energy and enthalpy) from the Southern to the Northern Hemisphere. Conversely, the lower branch then transports anomalous latent energy (LE) southward, leading to the southward precipitation shift they observed in gridded observations, in a reanalysis product, and in the ensemble mean of a subset of CMIP3/5 models. Similar changes in cross-equatorial transport in response to aerosols were found in CMIP5 historical simulations performed with all forcings, greenhouse gas–only forcing, and anthropogenic aerosol–only forcing (Allen et al. 2015; Irving et al. 2019; Lembo et al. 2019). Consistent with these results, Yukimoto et al. (2022) found that precipitation trends in the Northern Hemisphere were largely driven by changes in cross-equatorial heat transport associated with an anomalous Hadley circulation in historical simulations performed with the latest version of the Meteorological Research Institute Earth System Model (MRI-ESM2.0), and suggested that aerosol forcing may be the primary driver of hemispheric precipitation trends due to the impact on solar radiation.

In this study, we analyze the trends in poleward energy transport at all latitudes in a large ensemble of historical climate simulations. We find a significant northward anomaly in the total atmospheric plus oceanic transport from about 10°S to 40°N that peaks in approximately 1975. This anomaly occurs in each member of a large ensemble of historical climate simulations (Rodgers et al. 2021) performed with the Community Earth System Model, version 2 (Danabasoglu et al. 2020). Further investigation of a set of single-forcing simulations (Simpson et al. 2023) leads us to attribute this anomaly to historical emissions of SO_2 from Europe and North America that altered the meridional radiation gradient at the TOA through changes in the shortwave cloud radiative effect in the midlatitudes. We also find that the PET is much less sensitive to twenty-first-century SO_2 emissions from Asia, likely due to the increasing importance of cryosphere processes.

2. Methods

a. Data

Analysis is primarily performed on output from the CESM2 Large Ensemble (hereafter CESM2-LE; Rodgers et al. 2021). The CESM2-LE is a 100-member large ensemble that covers the period from 1850 to 2100 forced by the CMIP6 (Eyring et al. 2016) historical and SSP3-7.0 protocols. Fifty simulations from the large ensemble utilize the biomass burning (BMB) forcing from the CMIP6 protocol, which incorporates satellite observations of wildfires from 1997 to 2014, while the remaining 50 simulations utilize a smoothed BMB forcing designed to remove the abrupt change in interannual variability and nearly conserve total emissions (Rodgers et al. 2021; Fasullo et al. 2022). We have repeated our analysis for each of these two 50-member subensembles and found qualitatively similar results (not shown). The simulations with the smoothed BMB forcing had a slightly larger PET anomaly at certain latitudes in the Northern Hemisphere, but this difference was not found to be statistically significant during most years at most latitudes.

Our analysis is limited to the historical period (1850–2014), and we independently analyzed each of the 50 ensemble members which were forced by the smoothed BMB forcing prior to calculating ensemble-mean statistics. The CESM2-LE energy and moisture budgets were calculated from monthly mean radiation fields at the TOA and surface, and from monthly mean heat flux and precipitation fields at the surface. These budgets were used to calculate the atmospheric heat transport (AHT) using a polar cap integration method, described in the following section. The AHT was then added to the oceanic heat transport (OHT; directly output by the ocean model on monthly time scales and averaged to annual means) to give the total PET.

In addition to the CESM2-LE, we also analyze the CESM2 single forcing large ensemble (hereafter CESM2-SF; Simpson et al. 2023). The CESM2-SF uses an "only" approach in which each ensemble member is forced by one time-evolving forcing while all other forcings are held at 1850 levels. CESM2-SF includes four subensembles with between 15 and 20 members: 1) greenhouse gases (GHG); 2) anthropogenic aerosols (AER); 3), biomass burning (BMB, which uses the smoothed forcing described previously); and 4) "everything else" (EE). From the CESM2-SF, we are primarily interested in the AER subensemble in which only the "anthropogenic aerosol" forcing evolves in time, but analysis of the other subensembles is included for completeness. Again, our analysis is limited to the years 1850–2014.

Lastly, we also calculate the PET from the ERA5 atmospheric reanalysis (Hersbach et al. 2020). The ERA5 PET is then compared to the PET from the CESM2-LE and both exhibit similar behavior over their common time period of 1959–2014, although the ERA5 trend is smaller in magnitude.

b. *Poleward energy transport*

Neglecting marginal transports (e.g., rivers, groundwater flows, and icebergs), the poleward energy transport across an arbitrary latitude φ_0 can be calculated as the sum of AHT and OHT at that latitude.

The AHT can be calculated from a dynamic or an energetic perspective (Armour et al. 2019; Donohoe et al. 2020; Cox et al. 2022). In the dynamic perspective, the energy transports associated with fluid motions are integrated zonally and vertically throughout the depth of the atmosphere; from the energetic perspective the AHT is constrained by the fluxes of heat and radiation into the atmosphere at the TOA and the surface. The dynamic method allows for the decomposition of AHT into contributions from the mean meridional circulation and from eddies, but requires a much larger volume of data (e.g., 3D fields of temperature, humidity, and wind). For this study we calculate AHT from the energetic perspective to more easily analyze the heat transport in these large ensembles of climate simulations. Future work will utilize the dynamic perspective to investigate how historic forcing alters the heat transport associated with the mean and eddy components of the atmospheric circulation.

From the energetic perspective, the AHT can be calculated (e.g., Trenberth and Stepaniak 2003) by integrating the zonal mean time mean difference between the net energy flux at the TOA and at the surface,[1] from the South Pole to φ_0:

$$\overline{\mathrm{AHT}}^t(\varphi_0) = 2\pi a^2 \int_{-\pi/2}^{\varphi_0} \overline{F_T - F_S}^{t,\lambda} \cos\varphi' \, d\varphi', \qquad (1)$$

with the boundary condition

$$\overline{\mathrm{AHT}}^t(-\pi/2) = \overline{\mathrm{AHT}}^t(\pi/2) = 0. \qquad (2)$$

In Eq. (1), $\overline{\chi}^t$ denotes the time mean of a quantity χ, and $\overline{\chi}^{t,\lambda}$ denotes the zonal mean of the time mean of χ; F_T and F_S denote the net flux at the TOA and surface, respectively. The boundary condition at $\varphi = \pi/2$ is enforced by applying a uniform correction to the integrand to ensure that its global mean is zero.

Equation (1) is essentially an application of the divergence theorem. Under the assumption of no long-term heat uptake, which is valid for the atmosphere on time scales of a year or longer, the (vertical) convergence of energy from the TOA and surface into a "spherical cap" region defined by the limits of integration in Eq. (1) must be balanced by the (horizontal) divergence of energy from the cap. This represents the flux of energy across φ_0. A similar calculation yields the atmospheric LE transport if $\overline{F}^{t,\lambda}$ is replaced with difference between evaporation and precipitation, in energy units. Then, the total atmospheric transport minus LE transport gives the atmospheric DSE transport.

The assumption of no long-term heat uptake on yearly time scales *does not hold* for the ocean in the way that it does for the atmosphere. Then, a polar cap integration like Eq. (1) using $\overline{F_S}^{t,\lambda}$ would conflate oceanic heat transport and oceanic heat uptake. To avoid this, oceanic heat transport was not calculated from surface fluxes, but was instead taken directly from CESM2 ocean model monthly mean output (model field "N_HEAT"), interpolated onto the coarser atmospheric model grid, and averaged to annual means. The total poleward energy transport was then calculated as the sum of AHT plus OHT.

In practice, there is not a large difference between the PET calculated using the method described above and a simpler method of integrating the TOA energy balance, even though there has been a large amount of ocean heat uptake over the historical period (e.g., Huguenin et al. 2022). However, these two methods do give noticeably different results when applied to the CESM2-LE simulations under the SSP3-7.0 future forcing scenario (i.e., simulated years 2015–2100; not shown).

3. Results

a. *Climatology of PET in CESM2-LE*

Figure 1 shows the total poleward energy transport (black), the transport by the atmosphere and oceans (red and blue solid lines, respectively), and the atmospheric transport of latent energy and dry static energy (cyan and orange dashed lines for LE and DSE, respectively) from the CESM2-LE for the period from 1851 to 1900. The shading represents the 5th–95th percentile among ensemble members, as a measure of ensemble spread.

Figure 1 is consistent with previous studies of PET in the Earth system (e.g., Trenberth and Caron 2001; Yang et al. 2015). The

---

[1] This includes contributions from longwave and shortwave radiative fluxes, turbulent fluxes of heat and moisture from the surface to the atmosphere, and the heat flux associated with snowfall over oceans, although the contribution from this final term is an order of magnitude smaller than the other terms in the surface energy balance.

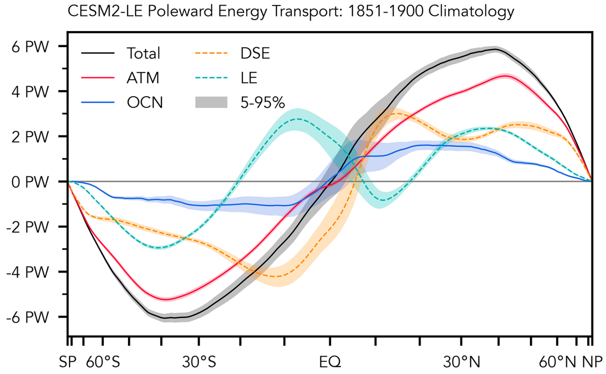

FIG. 1. CESM2-LE 1851–1900 ensemble mean zonally integrated northward energy transport (black) decomposed into contributions from the atmosphere (red) and oceans (blue). Atmospheric transport is further decomposed into dry static energy (orange) and latent energy (cyan) transports, in dashed lines. The shading around each line represents the 5th–95th percentile among ensemble members. Note that the horizontal axis is scaled by the sine of latitude.

total PET is a smooth, almost sinusoidal curve showing the transport of energy from the tropics to the poles, with peak values of almost 6 PW near 35° in each hemisphere. The constituent transports in the atmosphere and oceans are much less smooth, and yet they combine to give a total transport that is remarkably “seamless” (Trenberth and Stepaniak 2003) with latitude from the tropics to the extratropics. The spread in PET is clearly attributable to the spread in OHT, with very little variability evident in the AHT.

Broad characteristics of the atmospheric global circulation are evident in the curves for DSE and LE transport. In the tropics LE transport is equatorward, rather than poleward, due to the advection of moisture by the near-surface branches of the Hadley cells (Hwang et al. 2013; Yukimoto et al. 2022). This moisture convergence drives deep convection in the intertropical convergence zone (ITCZ) where energy is lifted and eventually exported poleward as DSE by the mean meridional circulation (Riehl and Malkus 1958; Neelin and Held 1987). Away from the equator transient and stationary eddies act to transport LE and DSE in the same direction. This eddy transport has been modeled as the simple downgradient diffusion of energy (Hwang and Frierson 2010; Siler et al. 2018; Armour et al. 2019; Lu et al. 2022).

b. Short-term variability in PET

The PET was calculated for each of the 50 CESM2-LE ensemble members with smoothed BMB for each year from 1851 to 2100. From this time series we then calculated the anomalous PET anomaly relative to the 1851–1900 ensemble mean climatology. The PET anomaly at each latitude from 1851 to 2014 is shown in the contours of Fig. 2. The contours show a combination of short-term and long-term variability, manifesting as vertical “pulses” lasting a few years on top of a decadal-scale trend of increasing and then decreasing PET anomaly. The high-frequency pulses are primarily due to oceanic heat transport variability (e.g., Trenberth and Fasullo 2017; Trenberth et al. 2019; Trenberth and Zhang 2019). This behavior is beyond the scope of this study, so a 5-yr Gaussian filter with a standard deviation of 1 year has been used to smooth this and subsequent time series in order to focus on the decadal-scale behavior: the lower-frequency variability (i.e., the right panel of Fig. 2) is the subject of the remainder of this study.

c. Long-term PET trends in CESM2-LE and ERA5

Perhaps more striking than the high-frequency pulses observed in Fig. 2 is the decadal-scale behavior. The PET anomaly shows a positive trend at most latitudes through the course of the twentieth century which reaches its largest magnitude of approximately +0.25 PW in the roughly rectangular region bounded by 10°S–40°N and 1965–90, consistent with the findings of Irving et al. (2019) and Lembo et al. (2019).

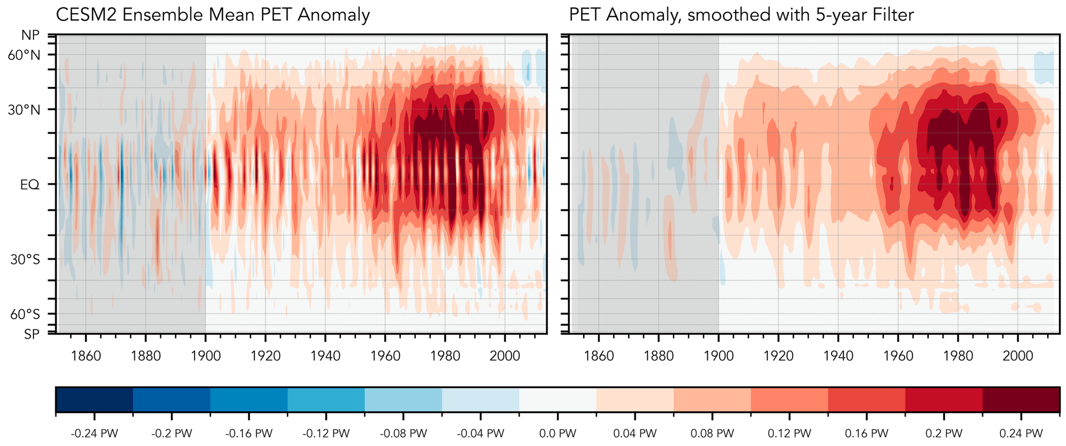

FIG. 2. (left) Ensemble mean anomalous total energy transport calculated as the sum of atmospheric and oceanic transports relative to the baseline (1851–1900, shaded in gray). Red shading indicates anomalous northward transport. Note that the vertical axis is scaled by the sine of latitude. (right) As in the left panel, but smoothed with a 5-yr Gaussian filter, as described in the text.

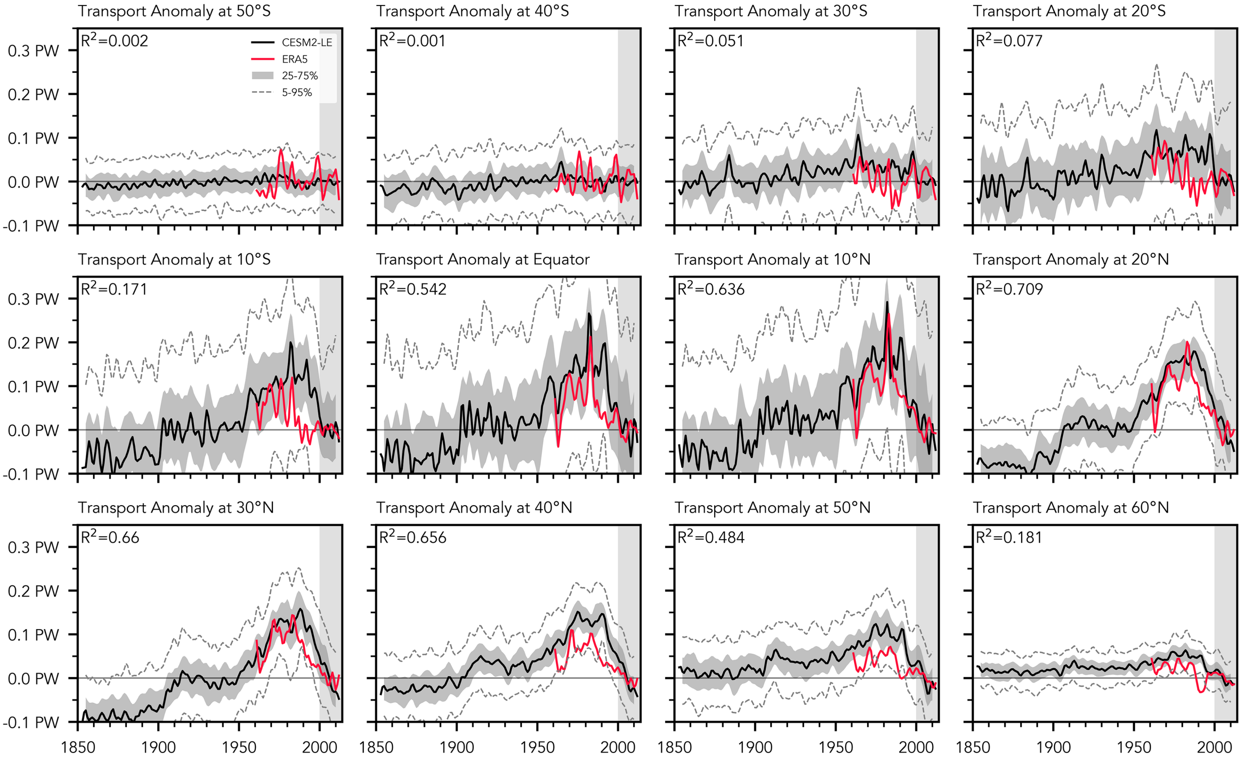

FIG. 3. Time series of anomalous energy transport (positive northward) at various latitudes. The CESM2-LE ensemble mean transport is shown in black, while the ERA5 transport is shown in red. The correlation coefficient between the ensemble mean CESM2-LE and ERA5 time series for their common period is shown in the top-left corner of each plot. Note that anomalies in this plot are relative to 2000–14 (shaded rectangular region).

To increase our confidence in the robustness of this trend, we calculate the PET from ERA5 atmospheric reanalyses for each full year of the ERA5 record (1959–2021). Due to the absence of an ocean model, we calculate the PET in the reanalysis following the energetic method by performing a polar cap integration on the annual mean TOA radiation fields calculated from monthly-mean reanalysis data. Anomalies were then calculated relative to a baseline, with the results shown in Fig. 3 alongside the CESM2-LE curves. The ERA5 data were smoothed using a 5-yr Gaussian filter, identical to the filter used on the CESM2-LE data. Note that for this figure the period 2000–14 was chosen as a common baseline for CESM2-LE and ERA5.

Each panel in Fig. 3 shows the PET anomaly (again, relative to 2000–14) at a particular latitude for ERA5 and CESM2-LE. The black curve shows the CESM2-LE ensemble mean. The shading around the black curve shows the 25th–75th percentile among CESM2-LE ensemble members, and the dashed gray lines represent the 5th–95th percentile. The red line shows the ERA5 anomaly. The correlation coefficient in the top-left corner is between the CESM2-LE ensemble mean and the ERA5 data for the common period. The primary conclusion from Fig. 3 is that the same PET anomaly is found in both the CESM2-LE and in ERA5. The ERA5 PET anomaly is of a similar magnitude and is moderately or highly correlated with the CESM2-LE anomaly from 10°S to 60°N (R^2 greater than 0.2, and as large as 0.7), even though the ERA5 data contain variability that is smoothed out in the ensemble mean of 50 members.

The PET trend at each latitude is quantified in Fig. 4 for both the CESM2-LE and for ERA5. The average PET anomaly at each latitude was calculated for the two 15-yr periods of 2000–14 and 1975–89. The difference between the two periods was then scaled by the time difference (i.e., 25 years) to give a

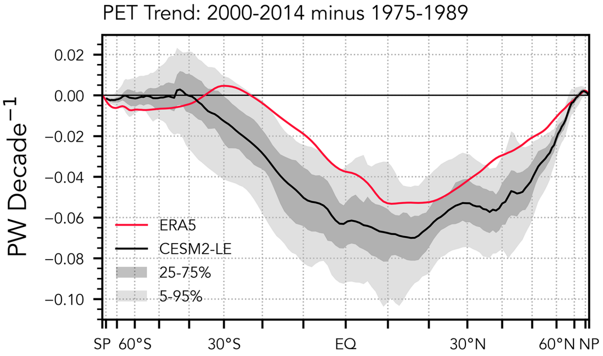

FIG. 4. Trend in PET at each latitude for CESM2-LE (black line; shading) and ERA5 (red line). The trend is calculated as the difference of the average of 2000–14 minus the average of 1975–89 using the smoothed time series.

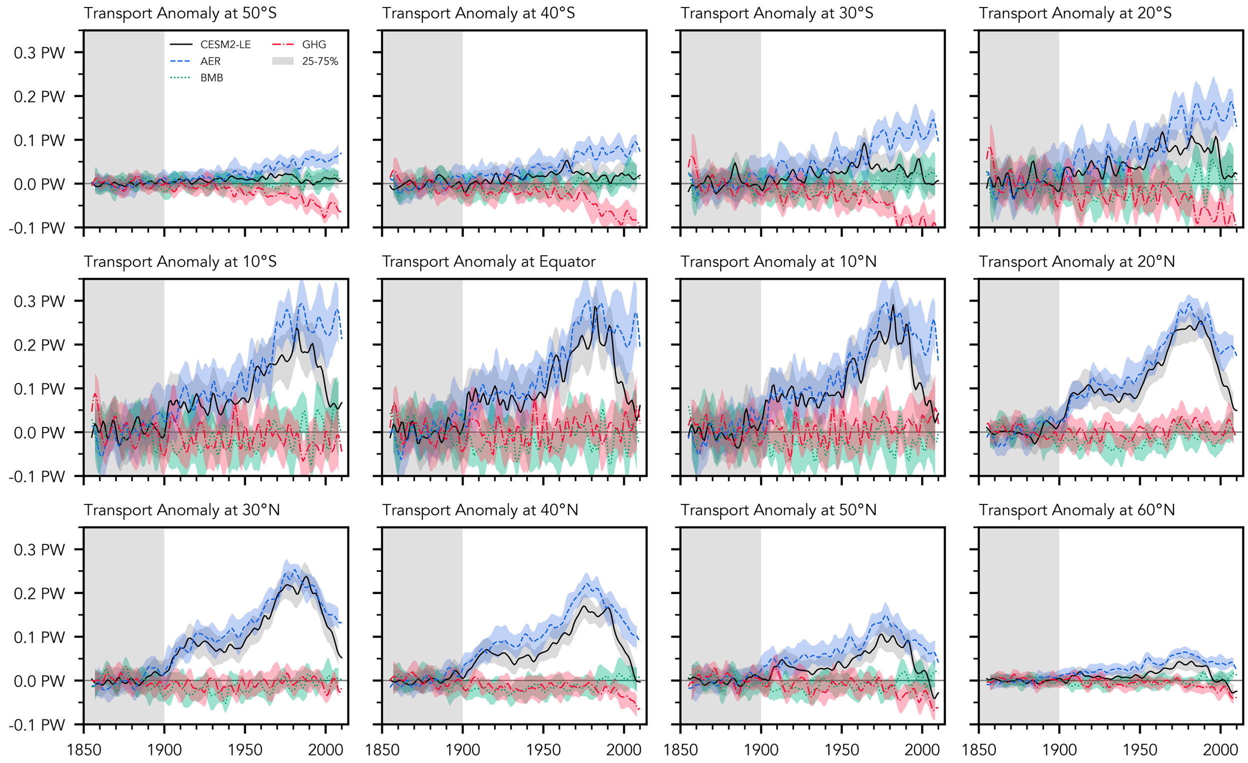

FIG. 5. As in Fig. 3, but for the comparison between the CESM2-LE and the CESM2-SF using the 1851–1900 baseline (shaded gray region).

PET trend in petawatts per decade. The shading once again represents the interquartile range or the 5th–95th percentile among CESM2-LE ensemble members.

From Fig. 4, the CESM2-LE appears to overestimate the PET at most latitudes: at the latitudes of interest (approximately 10°S–40°N) the magnitude of the ERA5 trend is occasionally smaller than the 5th percentile, and almost always smaller than the 25th percentile of ensemble members. However, the two curves are broadly similar, with the largest magnitude trend found between the equator and 20°N. The CESM2-LE trend here is about −0.07 PW per decade, while the ERA5 trend is about −0.05 PW per decade. Both curves show essentially zero trend poleward of about 70° in each hemisphere.

d. PET and SO_2 emissions

We now turn to the underlying cause of the twentieth-century PET anomaly. This anomaly occurs too early to result from anthropogenic greenhouse forcing or related effects (e.g., reduction in polar ice). Instead, our hypothesis is that this anomalous northward PET is due to anthropogenic SO_2 emissions.

To test this hypothesis we repeat our analysis using the CESM2 single forcing large ensemble (CESM2-SF; Simpson et al. 2023). The PET was calculated for each simulation in each subensemble (e.g., for each simulation with only AER forcing, or with only GHG forcing), with time series plots of the PET anomaly shown in Fig. 5 at various latitudes alongside the original CESM2-LE time series. The "everything else" (EE) ensemble does not show long-term trends and has been omitted for clarity. Again, a 5-yr Gaussian filter was applied to smooth out high-frequency variability.

The curves for the AER simulations (blue) show a similar PET anomaly that peaks around 1975 that is absent in the GHG (red) or the BMB (green) curves. In the Northern Hemisphere (e.g., 30°N), the blue AER curve almost exactly follows the black CESM2-LE curve. In the Southern Hemisphere (e.g., 30°S) the blue AER curve is larger than the CESM2-LE curve but is offset somewhat by the negative red GHG curve. This suggests some sort of linear cancellation in the PET response to forcing by aerosols and GHGs in the Southern Hemisphere that is not evident in the north.

At most latitudes and years, the curves associated with individual forcings add together to give the PET anomaly from the CESM2-LE ensemble mean (i.e., the red, blue, and green curves add together to give the black curve). The exception is from about 2000–14 and from 20°S to 20°N. Here, the anomaly in the AER simulations (blue) remains large and positive, the anomaly in the CESM2-LE simulations (black) decreases toward zero, and the anomaly in the GHG (red) and BMB (green) simulations is negative but is too small to counteract the AER simulations. The impact of the EE simulation is negligible here (not shown). This suggests that some nonlinear interaction between the various forcing agents reduces the PET anomaly in the first 15 years of the twenty-first century, which will be discussed in section 5.

As further support for the anthropogenic SO_2 hypothesis, Fig. 6 shows the SO_2 emissions from the Community Emissions

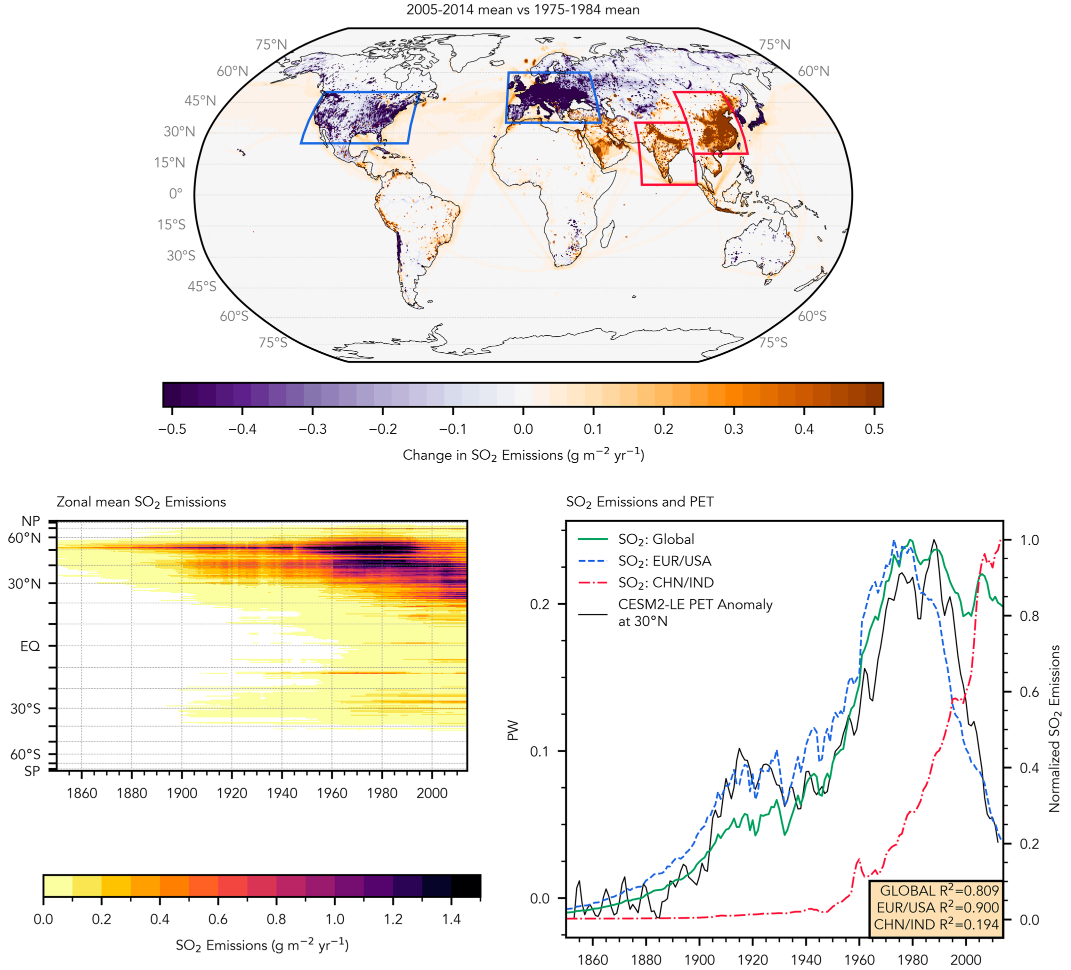

FIG. 6. (top) Difference between time-mean SO_2 emissions for 2005–14 minus 1975–84. (bottom left) Zonal mean SO_2 emissions from CEDS used as a contribution to the total anthropogenic aerosol forcing to the CESM2-LE. Values less than 0.01 $\mathrm{g\,m^{-2}\,yr^{-1}}$ masked. (bottom right) Time series of normalized global SO_2 emissions from CEDS (green line: global, blue dashed line: Europe and United States, red dash-dotted line: China and India), and ensemble mean CESM2-LE PET anomaly at 30°N (black line). Latitude and longitude limits for boxes drawn to define regions are included in the text.

Data System (CEDS; Hoesly et al. 2018), used as one of the forcings to the CESM2-LE and CESM2-SF AER simulations. These data provide an estimate of historical emissions and not of optical depth; however, the short lifetime of SO_2 implies a high level of correlation between SO_2 emissions and optical depth. The bottom-left panel shows a time series of the zonal mean SO_2 emissions from 1850 to 2014. There is a clear maximum centered around 50°N that peaks at about 1980 and decreases rapidly after about 1990. At the same time there is a secondary maximum centered around 40°N. After 1990, 40°N becomes the primary latitude of SO_2 emissions, and by the twenty-first century is joined by other maxima between 20° and 40°N.

The map in Fig. 6 shows the difference between the time-mean SO_2 emissions from the years 1975–84, and those of the years 2005–14. Purple (orange) colors show regions of reduced (increased) SO_2 emissions over the 30-yr period. The decrease seen in North America and Europe can be explained by a combination of air quality legislation, a shift from manufacturing to service-based economies, and the fall of the former Soviet Union. At the same time, the orange regions in China, India, Southeast Asia, and the Maritime Continent, as well as parts of the Middle East, are the consequence of rapid economic and population growth and increases in manufacturing (Hoesly et al. 2018). Also evident are increases in SO_2 emissions along prominent global shipping lanes.

The map and bottom-left panel show that the global SO_2 emissions did not simply peak and decrease over the historical period; instead, there is a complicated regional pattern and opposite trends in different regions. We now briefly investigate how those regional differences in SO_2 emissions correspond to the PET anomaly. The bottom-right panel of Fig. 6 shows the SO_2 emissions for the entire globe (green), combined emissions for Europe and the United States (EUR: 10°W–45°E,

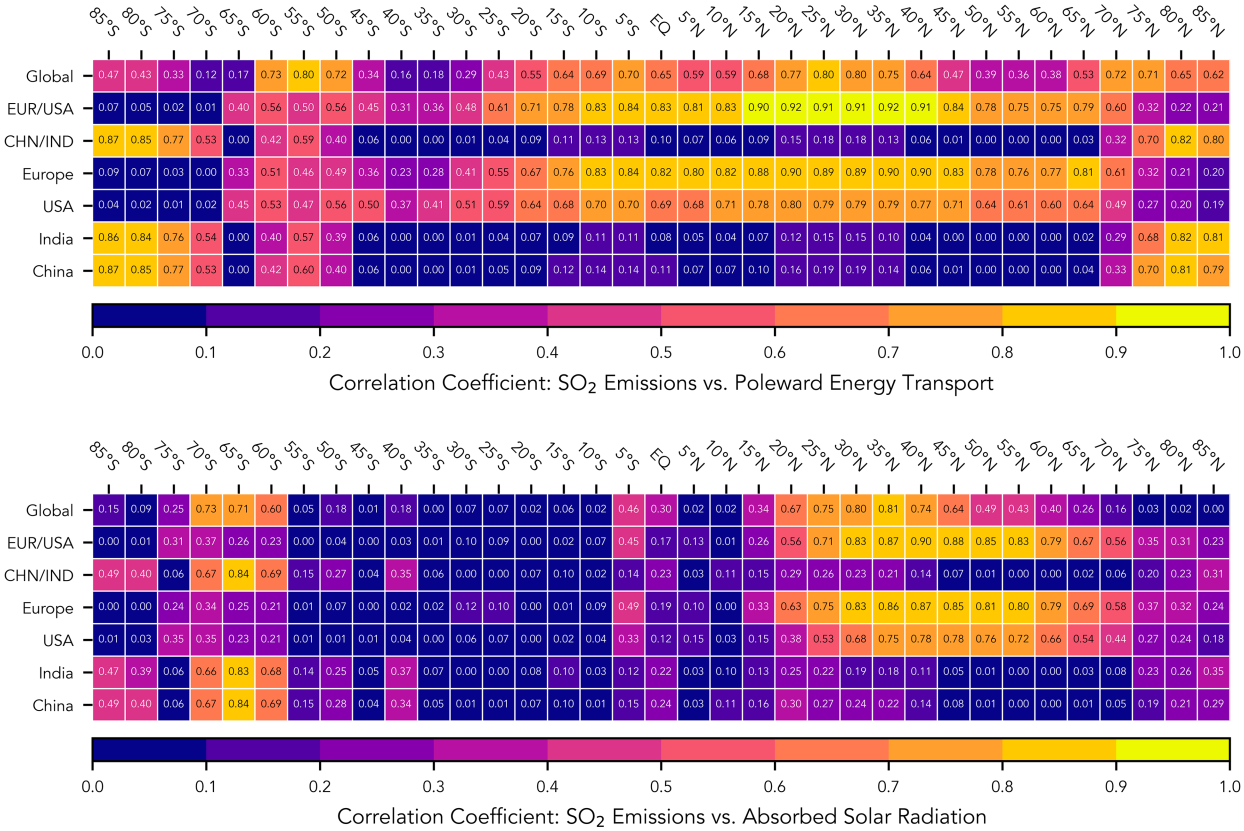

	85°S	80°S	75°S	70°S	65°S	60°S	55°S	50°S	45°S	40°S	35°S	30°S	25°S	20°S	15°S	10°S	5°S	EQ	5°N	10°N	15°N	20°N	25°N	30°N	35°N	40°N	45°N	50°N	55°N	60°N	65°N	70°N	75°N	80°N	85°N
Global	0.47	0.43	0.33	0.12	0.17	0.73	0.80	0.72	0.34	0.16	0.18	0.29	0.43	0.55	0.64	0.69	0.70	0.65	0.59	0.59	0.68	0.77	0.80	0.80	0.75	0.64	0.47	0.39	0.36	0.38	0.53	0.72	0.71	0.65	0.62
EUR/USA	0.07	0.05	0.02	0.01	0.40	0.56	0.50	0.56	0.45	0.31	0.36	0.48	0.61	0.71	0.78	0.83	0.84	0.83	0.81	0.83	0.90	0.92	0.91	0.91	0.92	0.91	0.84	0.78	0.75	0.75	0.79	0.60	0.32	0.22	0.21
CHN/IND	0.87	0.85	0.77	0.53	0.00	0.42	0.59	0.40	0.06	0.00	0.00	0.01	0.04	0.09	0.11	0.13	0.13	0.10	0.07	0.06	0.09	0.15	0.18	0.18	0.13	0.06	0.01	0.00	0.00	0.00	0.03	0.32	0.70	0.82	0.80
Europe	0.09	0.07	0.03	0.00	0.33	0.51	0.46	0.49	0.36	0.23	0.28	0.41	0.55	0.67	0.76	0.83	0.84	0.82	0.80	0.82	0.88	0.90	0.89	0.89	0.90	0.90	0.83	0.78	0.76	0.77	0.81	0.61	0.32	0.21	0.20
USA	0.04	0.02	0.01	0.02	0.45	0.53	0.47	0.56	0.50	0.37	0.41	0.51	0.59	0.64	0.68	0.70	0.70	0.69	0.68	0.71	0.78	0.80	0.79	0.79	0.79	0.77	0.71	0.64	0.61	0.60	0.64	0.49	0.27	0.20	0.19
India	0.86	0.84	0.76	0.54	0.00	0.40	0.57	0.39	0.06	0.00	0.00	0.01	0.04	0.07	0.09	0.11	0.11	0.08	0.05	0.04	0.07	0.12	0.15	0.15	0.10	0.04	0.00	0.00	0.00	0.00	0.02	0.29	0.68	0.82	0.81
China	0.87	0.85	0.77	0.53	0.00	0.42	0.60	0.40	0.06	0.00	0.00	0.01	0.05	0.09	0.12	0.14	0.14	0.11	0.07	0.07	0.10	0.16	0.19	0.19	0.14	0.06	0.01	0.00	0.00	0.00	0.04	0.33	0.70	0.81	0.79

Correlation Coefficient: SO_2 Emissions vs. Poleward Energy Transport

	85°S	80°S	75°S	70°S	65°S	60°S	55°S	50°S	45°S	40°S	35°S	30°S	25°S	20°S	15°S	10°S	5°S	EQ	5°N	10°N	15°N	20°N	25°N	30°N	35°N	40°N	45°N	50°N	55°N	60°N	65°N	70°N	75°N	80°N	85°N
Global	0.15	0.09	0.25	0.73	0.71	0.60	0.05	0.18	0.01	0.18	0.00	0.07	0.07	0.02	0.06	0.02	0.46	0.30	0.02	0.02	0.34	0.67	0.75	0.80	0.81	0.74	0.64	0.49	0.43	0.40	0.26	0.16	0.03	0.02	0.00
EUR/USA	0.00	0.01	0.31	0.37	0.26	0.23	0.00	0.04	0.00	0.03	0.01	0.10	0.09	0.00	0.02	0.07	0.45	0.17	0.13	0.01	0.26	0.56	0.71	0.83	0.87	0.90	0.88	0.85	0.83	0.79	0.67	0.56	0.35	0.31	0.23
CHN/IND	0.49	0.40	0.06	0.67	0.84	0.69	0.15	0.27	0.04	0.35	0.06	0.00	0.00	0.07	0.10	0.02	0.14	0.23	0.03	0.11	0.15	0.29	0.26	0.23	0.21	0.14	0.07	0.01	0.00	0.00	0.02	0.06	0.20	0.23	0.31
Europe	0.00	0.00	0.24	0.34	0.25	0.21	0.01	0.07	0.00	0.02	0.02	0.12	0.10	0.00	0.01	0.09	0.49	0.19	0.10	0.00	0.33	0.63	0.75	0.83	0.86	0.87	0.85	0.81	0.80	0.79	0.69	0.58	0.37	0.32	0.24
USA	0.01	0.03	0.35	0.35	0.23	0.21	0.01	0.01	0.01	0.04	0.00	0.06	0.07	0.00	0.02	0.04	0.33	0.12	0.15	0.03	0.15	0.38	0.53	0.68	0.75	0.78	0.78	0.76	0.72	0.66	0.54	0.44	0.27	0.24	0.18
India	0.47	0.39	0.06	0.66	0.83	0.68	0.14	0.25	0.05	0.37	0.07	0.00	0.00	0.08	0.10	0.03	0.12	0.22	0.03	0.10	0.13	0.25	0.22	0.19	0.18	0.11	0.05	0.01	0.00	0.00	0.03	0.08	0.23	0.26	0.35
China	0.49	0.40	0.06	0.67	0.84	0.69	0.15	0.28	0.04	0.34	0.05	0.01	0.01	0.07	0.10	0.01	0.15	0.24	0.03	0.11	0.16	0.30	0.27	0.24	0.22	0.14	0.08	0.01	0.00	0.00	0.01	0.05	0.19	0.21	0.29

Correlation Coefficient: SO_2 Emissions vs. Absorbed Solar Radiation

FIG. 7. Correlation between SO_2 emissions from various regions (rows) and (top) CESM2-LE ensemble mean PET (columns) and (bottom) CESM2-LE ensemble mean ASR (columns) at various latitudes. Shading in each cell represents the value of the R^2 correlation coefficient.

35°–60°N; USA: 125°–65°W, 25°–50°N; blue dashed line), and combined emissions for China and India (CHN: 95°–125°E, 20°–50°N; IND: 65°–95°E, 5°–35°N; red dash-dotted line). Emissions are normalized to give a maximum emission rate of 1. Also shown in black is the CESM2-LE ensemble mean PET anomaly at 30°N. From the beginning of the record through roughly 1975 the PET tracks closely with both the global emissions and emissions from only Europe and the United States (which made up the vast majority of emissions). After this period the green and blue curves diverge as SO_2 emissions decrease in the west and increase in other parts of the world, and the PET anomaly curve is highly correlated with the decline of emissions in Europe and North America ($R^2 = 0.91$). Throughout this time period the emissions from China and India are much less correlated with the PET anomaly ($R^2 = 0.18$) even though they combine to make up about half of global emissions by the end of the record. This is reminiscent of the work of Persad and Caldeira (2018), who showed that aerosol emissions from western Europe had a global cooling effect that was 14 times as strong as the same mass of aerosol emitted from India. The CHN/IND SO_2 emissions also mirror the ubiquitous CO_2 emission trend (e.g., Fig. 2 of Hoesly et al. 2018), a point we will return to in a few paragraphs.

To emphasize the robustness of the relationship between the PET anomaly and SO_2 emissions, the top table in Fig. 7 shows the correlation coefficient at every 5° of latitude between the CESM2-LE ensemble mean PET and the SO_2 emissions from various regions. This table shows that the correlations shown in the bottom-right panel of Fig. 6 are not outliers: the global emission trend shows moderate correlation with the PET anomaly at most nonpolar latitudes; the EUR/USA emissions are even more highly correlated, with $R^2 \geq 0.5$ for all latitudes between 25°S and 70°N; and the CHN/IND emissions are very *uncorrelated* with the PET anomaly at most latitudes equatorward of 65° in either hemisphere. The table also indicates that the emissions from Europe are slightly more correlated with the PET anomaly than those from the United States. It is unclear whether this is evidence of a stronger relationship between EUR emissions and PET or is merely the result of chance.

The table also shows a high degree of correlation between emissions from CHN/IND and the PET anomaly near the poles. However, the authors do not believe this is a real relationship for several reasons: 1) the CHN/IND emissions of SO_2 increase in a way that is reminiscent of the increase in CO_2, which is expected to lead to an increase in poleward energy transport (Hwang and Frierson 2010); 2) there is no obvious mechanism to explain how a Northern Hemispheric cooling from SO_2 emissions would lead to increased energy transport toward the South Pole; and 3) the PET anomaly at these

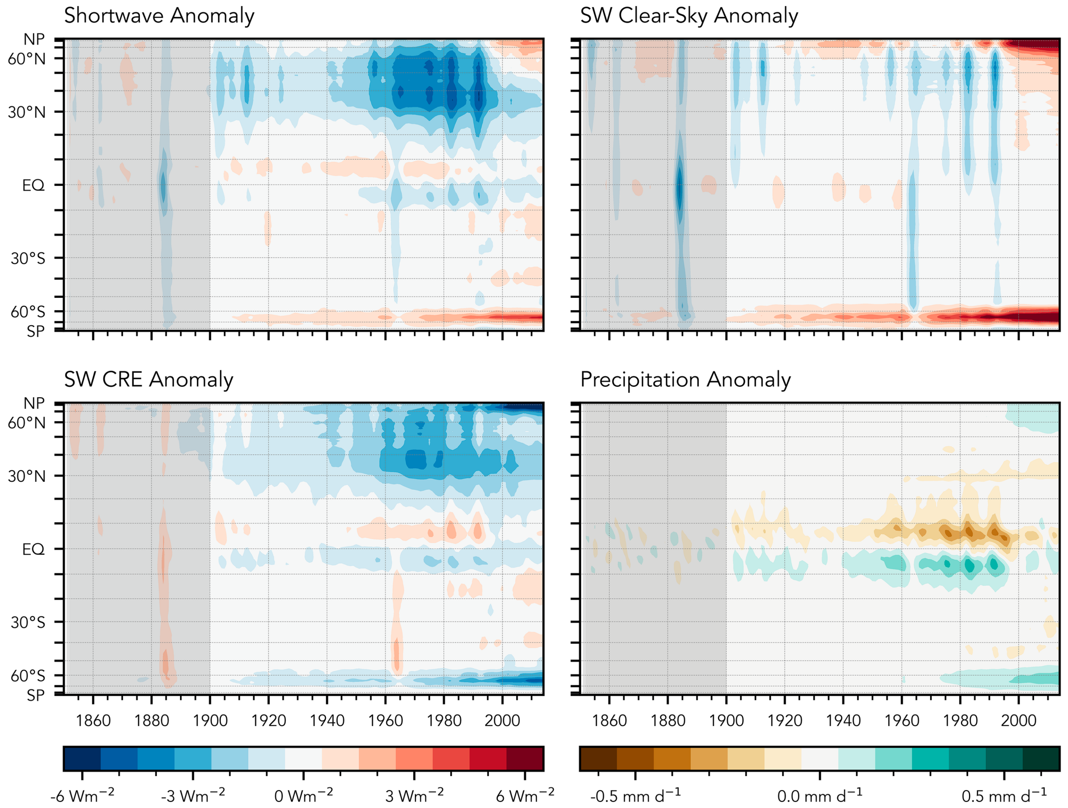

FIG. 8. (top left) Anomalous ensemble mean zonal mean shortwave flux at TOA, relative to 1851–1900 average. (top right) As in the top-left panel, but for the clear-sky shortwave flux at TOA. (bottom left) As in the top-left panel, but for the shortwave cloud radiative effect at the TOA (defined as full-sky minus clear-sky). (bottom right) As in the top-left panel, but for the total precipitation rate.

latitudes is at least an order of magnitude smaller than the PET anomaly near the equator (see Fig. 2).

The bottom table of Fig. 7 shows the correlation of SO_2 emissions with the zonal mean absorbed solar radiation (ASR, the difference between incoming and reflected shortwave radiation at the top of the atmosphere). Similar to our interpretation of the top table, we find that global SO_2 emissions are highly correlated ($R^2 = 0.8$) with the trend in ASR at a range of latitudes. These latitudes range from 20° to 60°N, encompassing the industrialized countries of the Northern Hemisphere. We will discuss this link between SO_2, PET, and ASR further in the following section.

4. Discussion

a. *Aerosol-radiative effects*

We have shown that historical SO_2 emissions from Europe and North America are highly correlated with the anomalous northward heat transport in the mid-to-late twentieth century. The exact way in which sulfate aerosols mediate changes in atmospheric and oceanic heat transports will be the subject of an upcoming study, but we briefly discuss one important component here.

Aerosol-radiative effects occur in the longwave, but are largest in the shortwave. The (typically smaller) aerosol direct effect describes the direct scattering of radiation by aerosols, while the (typically larger) aerosol indirect effect encompasses radiative impacts from aerosol-induced changes in clouds and precipitation (Twomey 1977; Albrecht 1989). We suspect that enhanced SO_2 emissions could have increased the reflection of shortwave radiation in the midlatitudes near the sources of emission, which would have increased the meridional albedo gradient. Following the argument of Stone (1978), the increased albedo gradient would imply an increase in northward energy transport to compensate for the reduction in absorbed shortwave radiation.

As a first look at this explanation, the CESM2-LE ensemble mean full-sky shortwave anomaly relative to 1851–1900 is shown in the top left panel of Fig. 8, along with the clear-sky anomaly (top right) and the shortwave cloud radiative effect (CRE; the difference between full-sky and clear-sky radiation; bottom left) (Ramanathan 1987; Allan 2011). The full-sky anomaly shows a perturbation between 30° and 60°N centered around 1975. This full-sky perturbation is similar to, but poleward of, the PET anomaly in Fig. 2: it increases steadily through the first half of the twentieth century, increases rapidly after WWII, peaks near 1975, and then decreases.

When comparing the clear-sky and CRE plots the perturbation is primarily from the shortwave CRE, suggesting that the

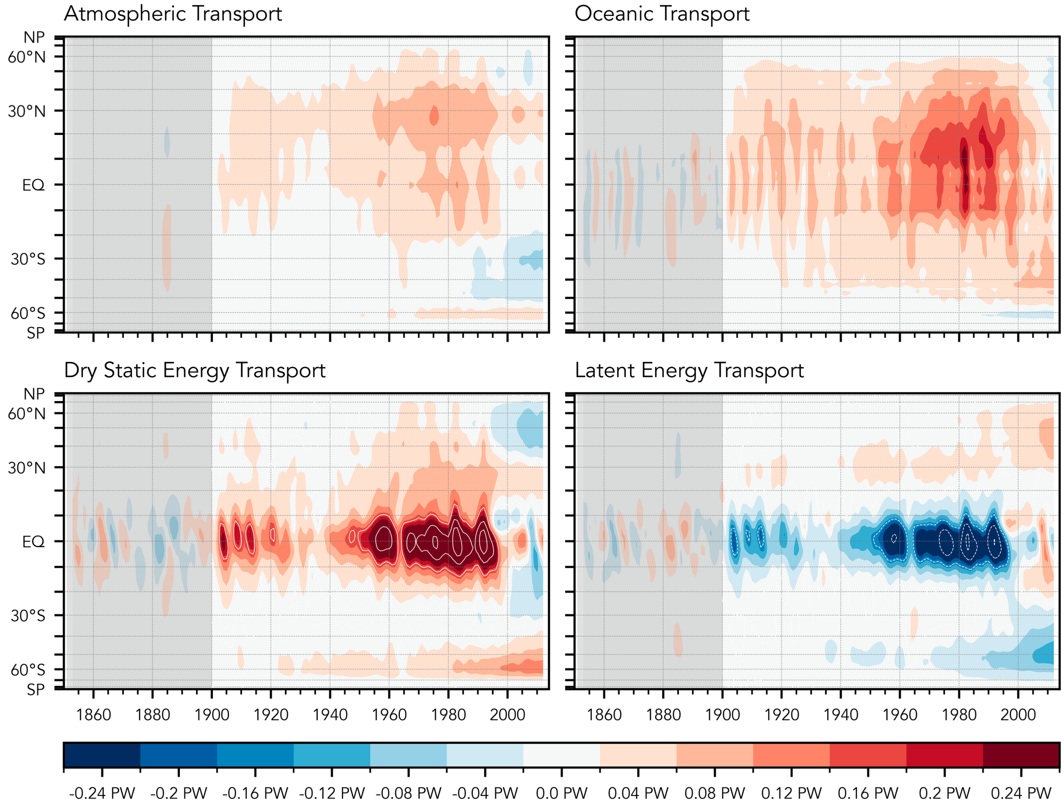

FIG. 9. As in Fig. 2, but for the four constituent transports in Fig. 1. The white contours in bottom panels are drawn in increments of ±0.16 PW, with negative values dashed. Note that these fields have also been smoothed with a 5-yr filter.

changes to the TOA shortwave balance—which lead to changes in the PET—are caused by aerosol cloud radiative effects rather than by the direct scattering of radiation. The largest signal in the clear-sky field prior to 2000 appears to be associated with high-frequency pulses associated with volcanoes. Eruptions inject sulfate aerosols into the stratosphere (Kremser et al. 2016), where there is not enough moisture to form optically thick clouds, compared to anthropogenic aerosols, which primarily remain in the troposphere and often serve as cloud condensation nuclei.

Of course, clouds are not the only aspect of the Earth system with the potential to alter the TOA shortwave balance. Another important component is Northern Hemisphere ice. A reduction in sea ice during the early twenty-first century may be the cause of the large *positive* shortwave anomaly found at northern high latitudes (see red shading in top-right corner of plots in the top row of Fig. 8). This *positive* ice-driven clear-sky anomaly occurred at the same time as SO_2 was primarily emitted from CHN/IND and acted to counteract the *negative* cloud radiative effect anomaly so that the total shortwave anomaly reduced in magnitude.

In the context of PET, these figures suggest that SO_2 emissions from Europe and North America led to changes in cloud properties near the latitude of emission (i.e., 30°–50°N). This different cloud regime increased the reflection of shortwave radiation back to space, which sharpened the meridional albedo gradient. The cooling associated with the reduction in solar absorption in the mid-latitudes led to an anomalous northward energy transport out of the tropics.

One obvious impact of the SO_2-induced changes in PET, first identified by Hwang et al. (2013) and reproduced here, can be seen in the bottom-right panel of Fig. 8, which shows the precipitation anomaly relative to the 1851–1900 baseline. The peak and subsequent reduction in SO_2 emissions in Europe and North America corresponds to a southward shift and eventual retreat of the zonal mean equatorial rainband associated with the ITCZ and the anomalous Hadley circulation (Hwang et al. 2013; Yukimoto et al. 2022).

b. *Partition of PET*

So far this study has focused on the total PET by the climate system. However, the partition of energy transport between the atmosphere and ocean is also of importance. These contributions are shown in the top row of Fig. 9, and time series at different latitudes are shown in Fig. 10.

The top panels of Fig. 9 indicate that the PET anomaly first illustrated in Fig. 2 is composed of changes to both AHT and OHT. These changes are of a similar magnitude, and a similar temporal behavior, although there are differences in the latitudinal structure. The AHT anomaly is largest in the Northern Hemisphere from 20° to 40°N. Away from the equator, it is

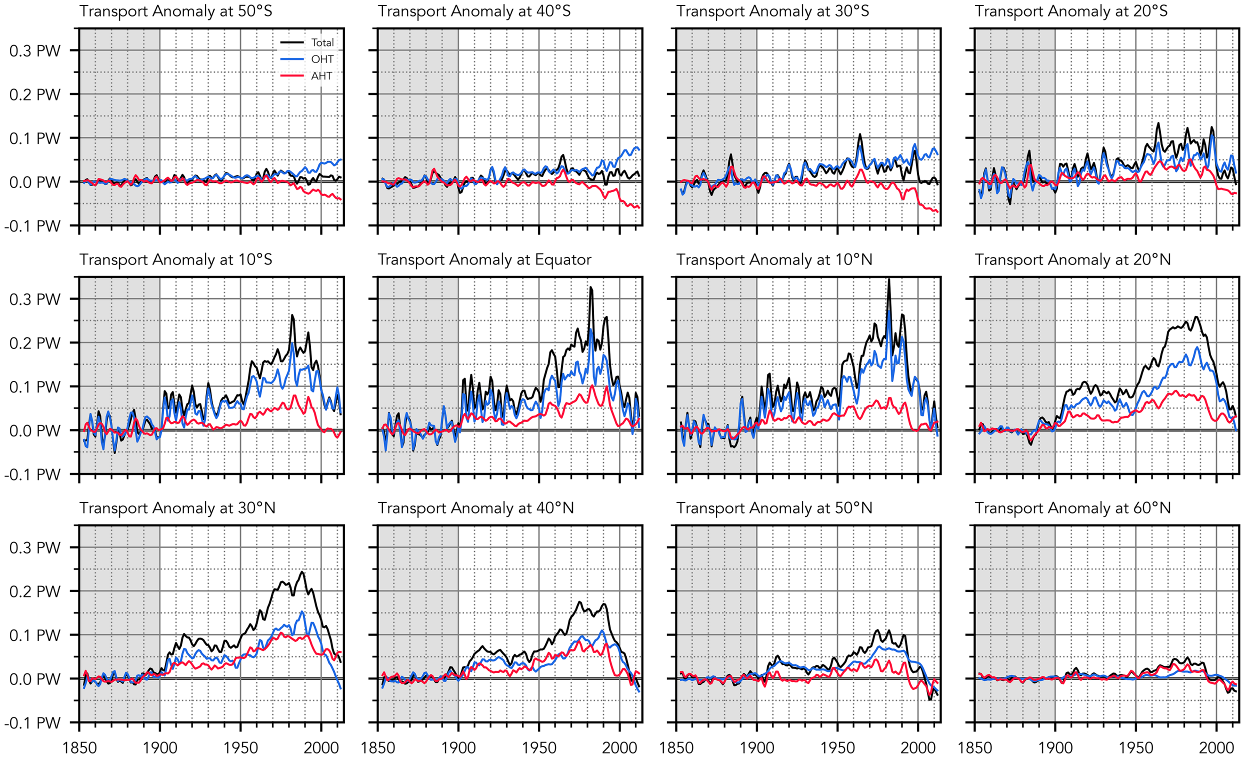

FIG. 10. Time series of PET (black), OHT (blue), and AHT (red) anomalies at various latitudes, relative to the 1851–1900 baseline, and smoothed by the 5-yr Gaussian filter.

known that the majority of the atmospheric energy transport is accomplished by stationary and transient eddies. This suggests that aerosol forcing may have increased the energy transport associated with eddies in CESM2, a possibility that will be investigated in future work.

The AHT anomaly at the equator is still large, if slightly smaller than the anomaly centered at 30°N. The further decomposition of AHT into dry static energy transport and latent energy transport (bottom row of Fig. 9) indicates that this anomaly is the residual of the much larger and offsetting anomalies in these two constituent transports. A southward ITCZ shift as seen in Fig. 8 is driven by an increase in southward latent energy transport (blue contours) associated with an anomalous Hadley circulation. This more southerly position allows the ITCZ to export more dry static energy to the north, consistent with the energetic understanding of ITCZ dynamics (Donohoe et al. 2013; Bischoff and Schneider 2014; Schneider et al. 2014; Adam et al. 2016).

The OHT anomaly appears to be somewhat larger than the AHT anomaly, with a magnitude in excess of 0.2 PW compared to 0.16 PW. This OHT anomaly is also consistent with previous analyses of CESM2 specifically and CMIP6 models more generally that have found an increase in the strength of the AMOC in response to aerosol forcing (Menary et al. 2020; Hassan et al. 2021; Robson et al. 2022; Simpson et al. 2023). This suggests that the OHT anomaly may be primarily due to changes in the AMOC.

The relative importance of the contributions to the total PET anomaly can be quantified by comparing the AHT and OHT time series at various latitudes in Fig. 10. From 10°S to 20°N the OHT anomaly (blue) is clearly larger than the AHT anomaly (red), sometimes by as much as a factor of 3. In contrast, at 20°S and from 30° to 50°N the AHT and OHT are approximately the same magnitude.

c. *Nonlinear relationship between PET, aerosol emissions, and the cryosphere*

Figure 6 raises an interesting question of why SO_2 emissions in the twenty-first century—primarily from China and South Asia—are not correlated with the PET in a similar way to twentieth-century emissions from Europe and North America. Here, we discuss several possible answers to this question.

One possibility is that the large quantity of black carbon emitted from China and India (Hoesly et al. 2018) offsets the shortwave effect of the sulfate aerosols during the final years of the historical period. Black carbon, primarily emitted from residential biomass burning for heating and cooking, is a strong absorber of shortwave radiation. It is conceivable, then, that the large quantity of black carbon emitted in the early years of the twenty-first century absorbed enough shortwave radiation to counteract the effect of SO_2 emissions. However, our results do not support this interpretation: the fact that the CESM2-SF AER simulations, which include black carbon alongside SO_2 (Simpson et al. 2023), do show a

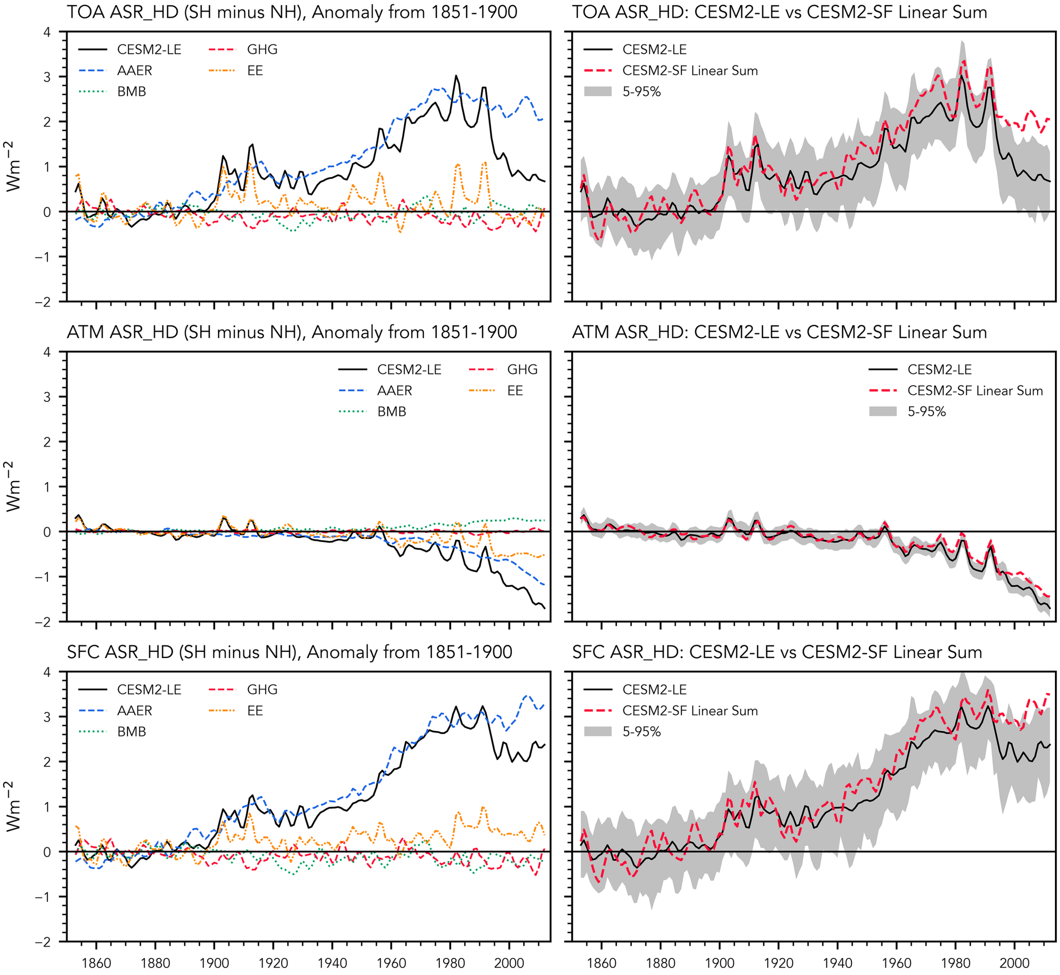

FIG. 11. Positive values indicate that the NH reflects more shortwave radiation than the SH. Note that the shading in the right panel shows the range between the 5th and 95th percentiles, in comparison to the interquartile range of earlier figures.

major PET anomaly in the twenty-first century suggests that a different emissions regime is not likely to be the cause of the disconnect between the SO_2 forcing and the PET anomaly.

In fact, the difference between the PET anomaly found in the full CESM2-LE simulations and the anomaly found in the CESM2-SF AER simulations is a key point. This indicates that the lack of a PET anomaly cannot be attributed to different responses to aerosols between the USA/EUR and IND/CHN regions (e.g., local cloud properties, latitude of emission, proximity to the AMOC, etc.) If these regional differences were the reason for the difference in the PET anomaly, then we would expect to see a much more rapid decrease in the PET anomaly in the AER simulations. Indeed, to first order, the PET anomaly in the AER simulations appears to largely follow the global SO_2 emission trend (cf. Fig. 5 and the bottom panel of Fig. 6).

Instead of considering regional differences in response to aerosol emissions, the question now becomes what other processes could lead to a reduction in the shortwave anomaly (Fig. 8). From about 1995 through 2014, the Northern Hemisphere shortwave anomaly becomes less negative, and even becomes positive in the northern high latitudes. A comparison of the other panels of Fig. 8 indicates that this reduction is primarily driven by a positive *clear-sky* shortwave anomaly, with only a small reduction in the magnitude of the negative CRE anomaly during these years. That this clear-sky shortwave anomaly is driven by a high-latitude process suggests a cryosphere process as the likely cause.

To quantify this change in the shortwave field, Fig. 11 shows the hemispheric difference in absorbed solar radiation (ASR_HD). The ASR_HD was found by calculating the area-weighted average of the net shortwave flux at the TOA in both hemispheres, and then taking the difference of the Southern minus the Northern Hemisphere (this convention was chosen so that anomalies are positive throughout the historical period). This calculation was repeated for the net shortwave flux at the surface, and the net shortwave absorption within the atmosphere.

Panels in the left column of Fig. 11 show the ASR_HD for the CESM2-LE and for each of the CESM2-SF subensembles;

the right panel shows the comparison between the CESM2-LE and a linear sum of the ensemble means of each of the CESM2-SF subensembles (e.g., AER + BMB + GHG + EE). The shading in the right column shows the 5th–95th percentile among CESM2-LE ensemble members.

The behavior of the curves in the left panel is quite similar to the analogous curves for the PET anomaly in Fig. 5. This is not surprising: the ASR_HD has previously been used as a rough metric for the AMOC (Menary et al. 2020; Robson et al. 2022), and thus its relevance to the total poleward energy transport is obvious due to the large amount of cross-equatorial heat transport in the Atlantic basin (Trenberth and Fasullo 2017; Trenberth et al. 2019; Forget and Ferreira 2019; Newsom et al. 2021). In the absence of changes in the outgoing longwave radiation, the ASR_HD determines the amount of cross-equatorial energy transport that is required to maintain hemispheric energy balance. If the anomaly in the ASR_HD is positive (which indicates a darker Southern Hemisphere), this implies a larger amount of energy must be transported northward across the equator, consistent with the PET anomaly found in this study.

The primary take-away from Fig. 11 is that the CESM2-LE ASR_HD is largely recreated from a linear sum of CESM2-SF subensembles from the beginning of the historical period until about 1995. After this point, the CESM2-LE curve drops rapidly, but the linear sum stays at about the same level (ignoring the large peaks clearly associated with the volcanic eruptions of Mt. Pinatubo and El Chichón in 1991 and 1982, respectively). This indicates a nonlinear response of the ASR_HD—and by extension the PET—to these climate forcings in CESM2 around the turn of the twenty-first century.

Comparison of the three panels in the right column indicates that this difference in ASR_HD between the CESM2-LE and the linear sum of CESM2-SF subensembles is driven by the surface component of the shortwave, again consistent with an impact from cryosphere processes. This complicated relationship between aerosol emissions, surface shortwave radiation, and the cryosphere in the CESM2-SF simulations was discussed in detail by Simpson et al. (2023). In particular, Simpson et al. (2023) described that the relationship between aerosol emissions and Northern Hemisphere ice was state dependent: the cryosphere responses to aerosols was different in a cooler climate where aerosols were emitted alone compared to a warmer climate where aerosols were emitted alongside greenhouse gases. They found that an imposed aerosol forcing in a climate *without* greenhouse gas warming increased the average snow cover by a larger amount than the same aerosol forcing in a climate *with* greenhouse warming. This leads to a larger surface albedo in the high latitudes of the cooler climate.

This state-dependent relationship appears to explain why the ASR_HD—and by extension the PET—from CESM2-LE is not recreated by a simple linear sum of the CESM2-SF subensembles from 2000 to 2014. This can be seen in the bottom panels of Fig. 11, where the linear sum of the ASR_HD from the CESM2-SF subensembles (red dashed line, right panel) is larger than the ASR_HD from the CESM2-LE simulations (black line, right panel), due to the contribution from the AER simulations (blue dashed line, left panel). In turn, this helps to explain why SO_2 emissions from India and China appear to have a smaller impact on the PET: the cryosphere processes counteract the shortwave impact of aerosols emitted from these regions. Cryosphere processes do not have the same impact during the last half of the twentieth century when emissions from Europe and North America were largest.

As an aside, our results for CESM2 are in contrast to those of Menary et al. (2020), who found that the ASR_HD in CMIP6 models was largely recreated from a linear sum of the ASR_HD in DAMIP simulations. This suggests that the rapid recovery in the PET anomaly after 1995 may be specific to CESM2, while the PET anomaly itself is likely a feature of a large number of CMIP6 models.

5. Conclusions

We have shown a robust link between historic anthropogenic SO_2 emissions and anomalous northward energy transport in the latter half of the twentieth century. Our study goes beyond previous studies which focused on the cross-equatorial transport to characterize the historic PET anomaly at all latitudes. This anomalous PET has been found in a large ensemble of climate simulations, a second ensemble of simulations forced only by historic anthropogenic aerosol emissions, as well as in an atmospheric reanalysis.

Consistent with previous studies, we find that Northern Hemisphere anthropogenic SO_2 emissions—specifically from Europe and North America—increased the reflection of shortwave radiation back to space, primarily due to aerosol–cloud interactions. By the early twenty-first century, the zonal mean shortwave anomaly (Fig. 8) had become much smaller; consequently, the PET anomaly (Fig. 2) decreased as well. Our results suggest that this reduction in the shortwave anomaly is due to the increasing importance of cryosphere processes around and after the turn of the twenty-first century, which complicates the simple relationship between SO_2 and PET found during the twentieth century.

Future work will explore the potential pathways that may explain how an increase in the reflection of shortwave radiation by midlatitude clouds leads to an increase in the total northward energy transport by the atmosphere and oceans. For the oceans, it is possible that anthropogenic emissions over land may alter the surface energy balance over oceans, downstream of the source of emissions. This possibility is reminiscent of previous work that has attempted to characterize the impact of aerosol emissions on tropical cyclones through the framework of tropical cyclone potential intensity (Sobel et al. 2019, and references therein). In principle, this downstream effect could lead to a stronger SST gradient and a larger amount of energy transport even without a change in the ocean currents. However, it appears that ocean currents do in fact change in CESM2 during the historical period: Simpson et al. (2023) found that the Atlantic meridional overturning circulation (AMOC) in CESM2 strengthened in response to historic forcing, largely driven by aerosol emissions.

The temporal evolution of the AMOC anomaly in the CESM2 Large Ensemble is quite similar to the PET anomaly discussed in this study [cf. Fig. 10 of Simpson et al. (2023) to Figs. 3 and 11 herein]. This is not surprising based on the amount of heat that is transported by the AMOC. We emphasize that the total PET anomaly discussed in this study cannot be immediately dismissed as a by-product of the CESM2 AMOC response to historical forcing. Perhaps one-third of the total heat transport anomaly is due to an increase in atmospheric transport, as shown in Figs. 9 and 10.

From an annual-mean, zonal-mean perspective the cross-equatorial AHT anomaly is likely driven by an anomalous Hadley circulation (Hwang et al. 2013; Yukimoto et al. 2022), and the AHT farther north is likely driven by changes in stationary and transient eddy heat transports. One possibility is that a reduction in absorbed shortwave radiation would increase the temperature difference between the tropics and the poles. Then, the energy transport would become more efficient, leading to an increase in energy transport without requiring a change in the winds. A related possibility is that a sharper temperature gradient would lead to stronger and/or more frequent baroclinic eddies in the midlatitude winters, which could transport more energy toward the poles. A clearer understanding of the PET trends in different seasons and in different regions is crucial to fully understand the historical behavior we have described.

Acknowledgments. The authors thank Professors Maria Rugenstein and Jeffery Pierce, both of Colorado State University, for helpful conversations which inspired additional lines of inquiry. We also thank the three anonymous reviewers for their comments that greatly improved this study. This work was supported by the National Oceanic and Atmospheric Administration through Grant NA19OAR4590155, and by the National Science Foundation through Grant AGS-1826643, both to the Colorado State University.

Data availability statement. Output from the CESM2-LE and CESM2-SF ensembles were accessed from the University Corporation for Atmospheric Research's GLADE file system. Information on the ensembles, including how to download data, may be found by following the links at https://www.cesm.ucar.edu/working-groups/climate/simulations. ERA5 reanalyses were downloaded from the ECMWF Copernicus Climate Data Store (CDS), at https://cds.climate.copernicus.eu/. SO_2 emissions data were downloaded from the Earth System Grid Federation https://esgf-node.llnl.gov/projects/cmip6/. CMIP6 "input4mips" forcing data (anthropogenic SO_2 emissions) are available from the Earth System Grid Federation at https://esgf-node.llnl.gov/projects/input4mips/.

REFERENCES

Acosta Navarro, J. C., and Coauthors, 2016: Amplification of Arctic warming by past air pollution reductions in Europe. *Nat. Geosci.*, **9**, 277–281, https://doi.org/10.1038/ngeo2673.

Adam, O., T. Bischoff, and T. Schneider, 2016: Seasonal and interannual variations of the energy flux equator and ITCZ. Part I: Zonally averaged ITCZ position. *J. Climate*, **29**, 3219–3230, https://doi.org/10.1175/JCLI-D-15-0512.1.

Aizawa, T., N. Oshima, and S. Yukimoto, 2022: Contributions of anthropogenic aerosol forcing and multidecadal internal variability to mid-20th century Arctic cooling—CMIP6/DAMIP multimodel analysis. *Geophys. Res. Lett.*, **49**, e2021GL097093, https://doi.org/10.1029/2021GL097093.

Albrecht, B. A., 1989: Aerosols, cloud microphysics, and fractional cloudiness. *Science*, **245**, 1227–1230, https://doi.org/10.1126/science.245.4923.1227.

Allan, R. P., 2011: Combining satellite data and models to estimate cloud radiative effect at the surface and in the atmosphere. *Meteor. Appl.*, **18**, 324–333, https://doi.org/10.1002/met.285.

Allen, R. J., A. T. Evan, and B. B. B. Booth, 2015: Interhemispheric aerosol radiative forcing and tropical precipitation shifts during the late twentieth century. *J. Climate*, **28**, 8219–8246, https://doi.org/10.1175/JCLI-D-15-0148.1.

Armour, K. C., N. Siler, A. Donohoe, and G. H. Roe, 2019: Meridional atmospheric heat transport constrained by energetics and mediated by large-scale diffusion. *J. Climate*, **32**, 3655–3680, https://doi.org/10.1175/JCLI-D-18-0563.1.

Bischoff, T., and T. Schneider, 2014: Energetic constraints on the position of the intertropical convergence zone. *J. Climate*, **27**, 4937–4951, https://doi.org/10.1175/JCLI-D-13-00650.1.

Bjerknes, J., 1964: Atlantic air-sea interaction. *Advances in Geophysics*, Vol. 10, Academic Press, 1–82, https://doi.org/10.1016/S0065-2687(08)60005-9.

Caesar, L., S. Rahmstorf, A. Robinson, G. Feulner, and V. Saba, 2018: Observed fingerprint of a weakening Atlantic Ocean overturning circulation. *Nature*, **556**, 191–196, https://doi.org/10.1038/s41586-018-0006-5.

——, G. D. McCarthy, D. J. R. Thornalley, N. Cahill, and S. Rahmstorf, 2021: Current Atlantic meridional overturning circulation weakest in last millennium. *Nat. Geosci.*, **14**, 118–120, https://doi.org/10.1038/s41561-021-00699-z.

Chiang, J. C. H., and C. M. Bitz, 2005: Influence of high latitude ice cover on the marine intertropical convergence zone. *Climate Dyn.*, **25**, 477–496, https://doi.org/10.1007/s00382-005-0040-5.

Cox, T., A. Donohoe, G. H. Roe, K. C. Armour, and D. M. W. Frierson, 2022: Near invariance of poleward atmospheric heat transport in response to midlatitude orography. *J. Climate*, **35**, 4099–4113, https://doi.org/10.1175/JCLI-D-21-0888.1.

Danabasoglu, G., and Coauthors, 2020: The Community Earth System Model version 2 (CESM2). *J. Adv. Model. Earth Syst.*, **12**, e2019MS001916, https://doi.org/10.1029/2019MS001916.

Deser, C., and Coauthors, 2020: Isolating the evolving contributions of anthropogenic aerosols and greenhouse gases: A new CESM1 large ensemble community resource. *J. Climate*, **33**, 7835–7858, https://doi.org/10.1175/JCLI-D-20-0123.1.

Donohoe, A., and A. Voigt, 2017: Why future shifts in tropical precipitation will likely be small: The location of the tropical rain belt and the hemispheric contrast of energy input to the atmosphere. *Climate Extremes: Patterns and Mechanisms*, *Geophys. Monogr.*, Vol. 226, Amer. Geophys. Union, 115–137, https://doi.org/10.1002/9781119068020.ch8.

——, J. Marshall, D. Ferreira, and D. McGee, 2013: The relationship between ITCZ location and cross-equatorial atmospheric heat transport: From the seasonal cycle to the last glacial maximum. *J. Climate*, **26**, 3597–3618, https://doi.org/10.1175/JCLI-D-12-00467.1.

——, K. C. Armour, G. H. Roe, D. S. Battisti, and L. Hahn, 2020: The partitioning of meridional heat transport from the last glacial maximum to CO_2 quadrupling in coupled climate models. *J. Climate*, **33**, 4141–4165, https://doi.org/10.1175/JCLI-D-19-0797.1.

Enderton, D., and J. Marshall, 2009: Explorations of atmosphere–ocean–ice climates on an aquaplanet and their meridional energy transports. *J. Atmos. Sci.*, **66**, 1593–1611, https://doi.org/10.1175/2008JAS2680.1.

England, M. R., I. Eisenman, N. J. Lutsko, and T. J. W. Wagner, 2021: The recent emergence of Arctic amplification. *Geophys. Res. Lett.*, **48**, e2021GL094086, https://doi.org/10.1029/2021GL094086.

Eyring, V., S. Bony, G. A. Meehl, C. A. Senior, B. Stevens, R. J. Stouffer, and K. E. Taylor, 2016: Overview of the Coupled Model Intercomparison Project Phase 6 (CMIP6) experimental design and organization. *Geosci. Model Dev.*, **9**, 1937–1958, https://doi.org/10.5194/gmd-9-1937-2016.

Fasullo, J. T., J.-F. Lamarque, C. Hannay, N. Rosenbloom, S. Tilmes, P. DeRepentigny, A. Jahn, and C. Deser, 2022: Spurious late historical-era warming in CESM2 driven by prescribed biomass burning emissions. *Geophys. Res. Lett.*, **49**, e2021GL097420, https://doi.org/10.1029/2021GL097420.

Forget, G., and D. Ferreira, 2019: Global ocean heat transport dominated by heat export from the tropical Pacific. *Nat. Geosci.*, **12**, 351–354, https://doi.org/10.1038/s41561-019-0333-7.

Frierson, D. M. W., and Coauthors, 2013: Contribution of ocean overturning circulation to tropical rainfall peak in the Northern Hemisphere. *Nat. Geosci.*, **6**, 940–944, https://doi.org/10.1038/ngeo1987.

Grennfelt, P., A. Engleryd, M. Forsius, Ø. Hov, H. Rodhe, and E. Cowling, 2020: Acid rain and air pollution: 50 years of progress in environmental science and policy. *Ambio*, **49**, 849–864, https://doi.org/10.1007/s13280-019-01244-4.

Gulev, S. K., and Coauthors, 2021: Changing state of the climate system. *Climate Change 2021: The Physical Science Basis*, V. Masson-Delmotte et al., Eds., Cambridge University Press, 287–422.

Hassan, T., R. J. Allen, W. Liu, and C. A. Randles, 2021: Anthropogenic aerosol forcing of the Atlantic meridional overturning circulation and the associated mechanisms in CMIP6 models. *Atmos. Chem. Phys.*, **21**, 5821–5846, https://doi.org/10.5194/acp-21-5821-2021.

Held, I. M., 2001: The partitioning of the poleward energy transport between the tropical ocean and atmosphere. *J. Atmos. Sci.*, **58**, 943–948, https://doi.org/10.1175/1520-0469(2001)058<0943:TPOTPE>2.0.CO;2.

——, and B. J. Soden, 2006: Robust responses of the hydrological cycle to global warming. *J. Climate*, **19**, 5686–5699, https://doi.org/10.1175/JCLI3990.1.

Hersbach, H., and Coauthors, 2020: The ERA5 global reanalysis. *Quart. J. Roy. Meteor. Soc.*, **146**, 1999–2049, https://doi.org/10.1002/qj.3803.

Hoesly, R. M., and Coauthors, 2018: Historical (1750–2014) anthropogenic emissions of reactive gases and aerosols from the Community Emissions Data System (CEDS). *Geosci. Model Dev.*, **11**, 369–408, https://doi.org/10.5194/gmd-11-369-2018.

Huang, Y., Y. Xia, and X. Tan, 2017: On the pattern of CO_2 radiative forcing and poleward energy transport. *J. Geophys. Res. Atmos.*, **122**, 10 578–10 593, https://doi.org/10.1002/2017JD027221.

Huguenin, M. F., R. M. Holmes, and M. H. England, 2022: Drivers and distribution of global ocean heat uptake over the last half century. *Nat. Commun.*, **13**, 4921, https://doi.org/10.1038/s41467-022-32540-5.

Hwang, Y.-T., and D. M. W. Frierson, 2010: Increasing atmospheric poleward energy transport with global warming. *Geophys. Res. Lett.*, **37**, L24807, https://doi.org/10.1029/2010GL045440.

——, ——, and J. E. Kay, 2011: Coupling between Arctic feedbacks and changes in poleward energy transport. *Geophys. Res. Lett.*, **38**, L17704, https://doi.org/10.1029/2011GL048546.

——, ——, and S. M. Kang, 2013: Anthropogenic sulfate aerosol and the southward shift of tropical precipitation in the late 20th century. *Geophys. Res. Lett.*, **40**, 2845–2850, https://doi.org/10.1002/grl.50502.

Irving, D. B., S. Wijffels, and J. A. Church, 2019: Anthropogenic aerosols, greenhouse gases, and the uptake, transport, and storage of excess heat in the climate system. *Geophys. Res. Lett.*, **46**, 4894–4903, https://doi.org/10.1029/2019GL082015.

Kang, S. M., 2020: Extratropical influence on the tropical rainfall distribution. *Curr. Climate Change Rep.*, **6**, 24–36, https://doi.org/10.1007/s40641-020-00154-y.

——, I. M. Held, D. M. W. Frierson, and M. Zhao, 2008: The response of the ITCZ to extratropical thermal forcing: Idealized slab-ocean experiments with a GCM. *J. Climate*, **21**, 3521–3532, https://doi.org/10.1175/2007JCLI2146.1.

Knietzsch, M.-A., A. Schröder, V. Lucarini, and F. Lunkeit, 2015: The impact of oceanic heat transport on the atmospheric circulation. *Earth Syst. Dyn.*, **6**, 591–615, https://doi.org/10.5194/esd-6-591-2015.

Kremser, S., and Coauthors, 2016: Stratospheric aerosol—Observations, processes, and impact on climate. *Rev. Geophys.*, **54**, 278–335, https://doi.org/10.1002/2015RG000511.

Larssen, T., and Coauthors, 2006: Acid rain in China. *Environ. Sci. Technol.*, **40**, 418–425, https://doi.org/10.1021/es0626133.

Lembo, V., D. Folini, M. Wild, and P. Lionello, 2019: Inter-hemispheric differences in energy budgets and cross-equatorial transport anomalies during the 20th century. *Climate Dyn.*, **53**, 115–135, https://doi.org/10.1007/s00382-018-4572-x.

Lu, J., W. Zhou, H. Kong, L. Ruby Leung, B. Harrop, and F. Song, 2022: On the diffusivity of moist static energy and implications for the polar amplification response to climate warming. *J. Climate*, **35**, 7127–7146, https://doi.org/10.1175/JCLI-D-21-0721.1.

Marshall, J., A. Donohoe, D. Ferreira, and D. McGee, 2013: The ocean's role in setting the mean position of the inter-tropical convergence zone. *Climate Dyn.*, **42**, 1967–1979, https://doi.org/10.1007/s00382-013-1767-z.

Menary, M. B., and Coauthors, 2020: Aerosol-forced AMOC changes in CMIP6 historical simulations. *Geophys. Res. Lett.*, **47**, e2020GL088166, https://doi.org/10.1029/2020GL088166.

Naik, V., and Coauthors, 2021: Short-lived climate forcers. *Climate Change 2021: The Physical Science Basis*, V. Masson-Delmotte et al., Eds., Cambridge University Press, 817–922.

Neelin, J. D., and I. M. Held, 1987: Modeling tropical convergence based on the moist static energy budget. *Mon. Wea. Rev.*, **115**, 3–12, https://doi.org/10.1175/1520-0493(1987)115<0003:MTCBOT>2.0.CO;2.

Newsom, E. R., A. F. Thompson, J. F. Adkins, and E. D. Galbraith, 2021: A hemispheric asymmetry in poleward ocean heat transport across climates: Implications for overturning and polar warming. *Earth Planet. Sci. Lett.*, **568**, 117033, https://doi.org/10.1016/j.epsl.2021.117033.

Oort, A. H., 1971: The observed annual cycle in the meridional transport of atmospheric energy. *J. Atmos. Sci.*, **28**, 325–339, https://doi.org/10.1175/1520-0469(1971)028<0325:TOACIT>2.0.CO;2.

Persad, G. G., and K. Caldeira, 2018: Divergent global-scale temperature effects from identical aerosols emitted in different regions. *Nat. Commun.*, **9**, 3289, https://doi.org/10.1038/s41467-018-05838-6.

Pithan, F., and T. Jung, 2021: Arctic amplification of precipitation changes—The energy hypothesis. *Geophys. Res. Lett.*, **48**, e2021GL094977, https://doi.org/10.1029/2021GL094977.

Previdi, M., K. L. Smith, and L. M. Polvani, 2021: Arctic amplification of climate change: A review of underlying mechanisms. *Environ. Res. Lett.*, **16**, 093003, https://doi.org/10.1088/1748-9326/ac1c29.

Rahmstorf, S., J. E. Box, G. Feulner, M. E. Mann, A. Robinson, S. Rutherford, and E. J. Schaffernicht, 2015: Exceptional twentieth-century slowdown in Atlantic Ocean overturning circulation. *Nat. Climate Change*, **5**, 475–480, https://doi.org/10.1038/nclimate2554.

Ramanathan, V., 1987: The role of Earth radiation budget studies in climate and general circulation research. *J. Geophys. Res.*, **92**, 4075–4095, https://doi.org/10.1029/JD092iD04p04075.

Riehl, H., and J. S. Malkus, 1958: On the heat balance in the equatorial trough zone. *Geophysica*, **6**, 503–537.

Robson, J., and Coauthors, 2022: The role of anthropogenic aerosol forcing in the 1850–1985 strengthening of the AMOC in CMIP6 historical simulations. *J. Climate*, **35**, 6843–6863, https://doi.org/10.1175/JCLI-D-22-0124.1.

Rodgers, K. B., and Coauthors, 2021: Ubiquity of human-induced changes in climate variability. *Earth Syst. Dyn.*, **12**, 1393–1411, https://doi.org/10.5194/esd-12-1393-2021.

Rose, B. E. J., and D. Ferreira, 2012: Ocean heat transport and water vapor greenhouse in a warm equable climate: A new look at the low gradient paradox. *J. Climate*, **26**, 2117–2136, https://doi.org/10.1175/JCLI-D-11-00547.1.

Rosenfeld, D., and Coauthors, 2014: Global observations of aerosol-cloud-precipitation-climate interactions. *Rev. Geophys.*, **52**, 750–808, https://doi.org/10.1002/2013RG000441.

Schneider, T., T. Bischoff, and G. H. Haug, 2014: Migrations and dynamics of the intertropical convergence zone. *Nature*, **513**, 45–53, https://doi.org/10.1038/nature13636.

Screen, J. A., C. Deser, and I. Simmonds, 2012: Local and remote controls on observed Arctic warming. *Geophys. Res. Lett.*, **39**, L10709, https://doi.org/10.1029/2012GL051598.

Serreze, M. C., and R. G. Barry, 2011: Processes and impacts of Arctic amplification: A research synthesis. *Global Planet. Change*, **77**, 85–96, https://doi.org/10.1016/j.gloplacha.2011.03.004.

Shaw, T. A., and Z. Smith, 2022: The midlatitude response to polar sea ice loss: Idealized slab-ocean aquaplanet experiments with thermodynamic sea ice. *J. Climate*, **35**, 2633–2649, https://doi.org/10.1175/JCLI-D-21-0508.1.

Shindell, D., M. Schulz, Y. Ming, T. Takemura, G. Faluvegi, and V. Ramaswamy, 2010: Spatial scales of climate response to inhomogeneous radiative forcing. *J. Geophys. Res.*, **115**, D19110, https://doi.org/10.1029/2010JD014108.

Siler, N., G. H. Roe, and K. C. Armour, 2018: Insights into the zonal-mean response of the hydrologic cycle to global warming from a diffusive energy balance model. *J. Climate*, **31**, 7481–7493, https://doi.org/10.1175/JCLI-D-18-0081.1.

Simpson, I. R., and Coauthors, 2023: The CESM2 single forcing large ensemble and comparison to CESM1: Implications for experimental design. *J. Climate*, **36**, 5687–5711, https://doi.org/10.1175/JCLI-D-22-0666.1.

Sobel, A. H., S. J. Camargo, and M. Previdi, 2019: Aerosol versus greenhouse gas effects on tropical cyclone potential intensity and the hydrologic cycle. *J. Climate*, **32**, 5511–5527, https://doi.org/10.1175/JCLI-D-18-0357.1.

Stone, P. H., 1978: Constraints on dynamical transports of energy on a spherical planet. *Dyn. Atmos. Oceans*, **2**, 123–139, https://doi.org/10.1016/0377-0265(78)90006-4.

Sverdrup, H. U., M. W. Johnson, and R. H. Fleming, 1942: *The Oceans: Their Physics, Chemistry, and General Biology*. Prentice-Hall, 1087 pp.

Trenberth, K. E., 1979: Mean annual poleward energy transports by the oceans in the Southern Hemisphere. *Dyn. Atmos. Oceans*, **4**, 57–64, https://doi.org/10.1016/0377-0265(79)90052-6.

——, and J. M. Caron, 2001: Estimates of meridional atmosphere and ocean heat transports. *J. Climate*, **14**, 3433–3443, https://doi.org/10.1175/1520-0442(2001)014<3433:EOMAAO>2.0.CO;2.

——, and D. P. Stepaniak, 2003: Seamless poleward atmospheric energy transports and implications for the Hadley circulation. *J. Climate*, **16**, 3706–3722, https://doi.org/10.1175/1520-0442(2003)016<3706:SPAETA>2.0.CO;2.

——, and ——, 2004: The flow of energy through the Earth's climate system. *Quart. J. Roy. Meteor. Soc.*, **130**, 2677–2701, https://doi.org/10.1256/qj.04.83.

——, and J. T. Fasullo, 2017: Atlantic meridional heat transports computed from balancing Earth's energy locally. *Geophys. Res. Lett.*, **44**, 1919–1927, https://doi.org/10.1002/2016GL072475.

——, and Y. Zhang, 2019: Observed interhemispheric meridional heat transports and the role of the Indonesian Throughflow in the Pacific Ocean. *J. Climate*, **32**, 8523–8536, https://doi.org/10.1175/JCLI-D-19-0465.1.

——, ——, J. T. Fasullo, and L. Cheng, 2019: Observation-based estimates of global and basin ocean meridional heat transport time series. *J. Climate*, **32**, 4567–4583, https://doi.org/10.1175/JCLI-D-18-0872.1.

Twomey, S., 1977: The influence of pollution on the shortwave albedo of clouds. *J. Atmos. Sci.*, **34**, 1149–1152, https://doi.org/10.1175/1520-0469(1977)034<1149:TIOPOT>2.0.CO;2.

Vonder Haar, T. H., and A. H. Oort, 1973: New estimate of annual poleward energy transport by Northern Hemisphere oceans. *J. Phys. Oceanogr.*, **3**, 169–172, https://doi.org/10.1175/1520-0485(1973)003<0169:NEOAPE>2.0.CO;2.

Yang, H., Q. Li, K. Wang, Y. Sun, and D. Sun, 2015: Decomposing the meridional heat transport in the climate system. *Climate Dyn.*, **44**, 2751–2768, https://doi.org/10.1007/s00382-014-2380-5.

Yukimoto, S., N. Oshima, H. Kawai, M. Deushi, and T. Aizawa, 2022: Role of interhemispheric heat transport and global atmospheric cooling in multidecadal trends of Northern Hemisphere precipitation. *Geophys. Res. Lett.*, **49**, e2022GL100335, https://doi.org/10.1029/2022GL100335.